Accepted Manuscript. Reference : EPSL, 308 (2011) 141–150

Spatiotemporal evolution of surface creep in the Parkfield region of the San Andreas Fault (1993–2004) from synthetic aperture radar.

M. de Michele[a*], D. Raucoules[a], F. Rolandone[b], P. Briole[c], J. Salichon[d], A. Lemoine[a], H. Aochi[a]

[a]French Geological Survey (BRGM), 3 Av. C. Guillemin, 45060 Orléans Cédex 2, France.
[b]ISTEP, CNRS UMR 7193, Université Pierre et Marie Curie, Paris VI, 4, Place Jussieu, Paris Cédex 05, France.
[c]Laboratoire de Géologie, CNRS UMR 8538, Ecole Normale Supérieure, 24 Rue Lhomond, 75231 Paris Cédex 05, France.
[d]Institut National des Sciences de l'Univers, Géosciences Azur, UMR-6526, 250 rue Albert Einstein, Les Lucioles 1, Sophia Antipolis, 06560 Valbonne, France.

Abbreviated title:
Spatiotemporal evolution of surface creep at Parkfield from InSAR.

Abstract

The Parkfield section of the San Andreas Fault (SAF) is defined as a transitional portion of the fault between slip-release behavior types in the creeping section of the SAF to the northwest and the apparently locked section to the southeast. The Parkfield section is characterized by complex frictional fault behavior because it represents a transition zone from aseismic creep to stick-slip regime. At least six historic earthquakes of M_w ~6 have occurred in this area in 1881, 1901, 1922, 1934, 1966, and 2004. It was observed in the 2004 M_w 6.0 Parkfield earthquake that ~70% of the total (coseismic and postseismic) moment release occurred aseismically. To understand the SAF behavior in this area, it is of particular interest to measure and analyze, not only the spatial evolution of the surface displacement in this area, but also its evolution over time. Using radar data acquired by the European Space Agency's European Remote Sensing (ERS1-2) satellites, we constructed descending interferograms and retrieved time series of surface displacements along the central SAF for the decade preceding the 2004 Parkfield earthquake. We focus on characterizing the space and time evolution of surface creep in the Parkfield and Cholame sections. The spatial pattern of the interseismic displacement rate indicates that tectonic strain was not uniformly distributed along the strike of the fault between 1993 and 2004. **Our data indicate** not only a decrease in the creep rate from the Parkfield section to south of Highway-46 from 1.4 ±0.3 cm/y to 0.6 ±0.3 cm/y, but also a small but significant creep-rate increase in the Cholame section to 0.2 ±0.1 cm/y. The evidence **for** episodic creep in the Cholame section of the SAF south-east of Parkfield is in contrast with previously published interpretations of GPS and trilateration data. The Cholame section of the SAF merits close monitoring because it was **likely the nucleation site** of the 1857 Fort Tejón earthquake and because it has shown recent evidence of deep slow slip as revealed by deep tremors.

Introduction

The Parkfield section of the San Andreas Fault (SAF) (Fig. 1) lies at the boundary between the creeping section to the northwest, which **slips** steadily at a rate of 25–30 mm/y (**e.g.** Lisowski and Prescott, 1981; Titus et al., 2005, 2006; Rolandone et al., 2008) and sections to the southeast that are considered locked and last ruptured in the 1857 M_w 7.9 Fort Tejón earthquake (McEvilly et al., 1967; Sieh, 1978). The Parkfield section is characterized by the occurrence of M_w ~6 earthquakes with short recurrence times (e.g., Roeloffs and Langbein, 1994; Bakun et al., 2005). At least six historic earthquakes of M_w ~6 occurred in this area in 1881, 1901, 1922, 1934, 1966, and 2004. Recent studies based on paleoseismology and statistical seismology suggest that the locked section to the southeast displays a quasi-periodic century-long time interval between earthquakes (Scharer et al., 2010; Akçiz et al., 2010).

The Parkfield section is a transition zone from aseismic creep to stick-slip regime characterized by complex frictional fault behaviour. It exhibits mixed mechanical behaviour: creep at the surface and locked asperities at mid-seismogenic depths (Harris and Segall, 1987; Murray et al., 2001). Surface creep rates decrease from ~28 mm/y in the central creeping section (e.g., Titus et al., 2006, Rolandone et al., 2008) to ~0 mm/y in the Cholame section (e.g., Lienkaemper and Prescott, 1989; Murray et al., 2001). In the Parkfield section, creepmeters and alignment arrays indicate that shallow slip occurs by means of millimeter- to centimeter-scale episodic creep events, as well as by intervening steady slip (e.g., Burford and Harsh, 1980; Lisowski and Prescott, 1981). Slow slip transients of varying duration and magnitude are also well documented (Langbein et al., 1999; Murray and Segall, 2005). Nadeau and McEvilly (1999) showed slip accelerations around the Parkfield asperity from observations of repeating identical earthquake sequences initiating in 1992; these accelerations were confirmed by two-color electronic distance measurements (EDM) (Langbein et al., 1999; Gao et al., 2000). During the last Parkfield earthquake in 2004 (M_w 6.0), approximately 70% of the total (coseismic and postseismic) moment release occurred aseismically (Johanson et al., 2006). Bakun and McEvilly (1984) predicted that

the next ~M6 earthquake at Parkfield would occur in 1988 ±5 years, but the Parkfield earthquake occurred in September 2004. The previous event was in 1966, making the interseismic period between the 1966 and 2004 earthquakes the longest **in the historical record** (Bakun and McEvilly, 1984; Roeloffs and Langbein, 1994). In this context, it is of particular interest to measure and analyze not only the spatial evolution of interseismic surface displacement in the Parkfield area, but also its evolution over time. For this purpose, we have used the InSAR technique to derive time series of surface displacements. Along the SAF, InSAR has **previously** been used to detect aseismic slip (e.g., Rosen et al., 1988; Lyon and Sandwell, 2003; Johanson and Bürgmann, 2005) and interseismic strain buildup (Fialko, 2006, Lundgren et al., 2009). Ryder and Bürgmann (2008) stacked 12 differential interferograms spanning 1992 to 2000 to measure spatial variations in creep rate along the creeping section of the SAF, northwest of **the town of** Parkfield. Johanson and Bürgmann (2005) investigated the distribution of interseismic creep in the northern transition zone of the creeping segment at San Juan Bautista. The current study focuses on the transition section of the SAF, between the town of Parkfield and southeast of highway-46, where slip **behavior** is assumed to decay from steady creep to locked conditions.

In this article, we first present the InSAR methodology. We concentrate on the InSAR measurement of surface displacement over the decade before the September 28, 2004, Parkfield event. Next, we discuss the spatiotemporal evolution of the surface displacement field of the SAF along the Parkfield and Cholame sections. Then, we compare our results to field measurements such as EDM, creepmeters and alignment arrays as well as seismicity at depth. In particular, we obtain insights to answer the following questions; how surface creep varies spatially and temporally along the Parkfield and Cholame sections of the SAF **and** how microseismicity correlates with variations in the spatiotemporal surface creep behaviour?

2. Methodology

ERS1-2 InSAR can map ground deformation at a spatial resolution of tens of meters with subcentimeter precision in the line-of-sight direction (LOS) of the satellite (e.g., Massonnet and Feigl, 1998). We acquired all available ERS1-2 archived data for the Parkfield area before the September 28, 2004, Parkfield earthquake. We chose to process the descending orbit ERS1-2 acquisitions to obtain a better InSAR LOS sensitivity to strike-slip surface movement parallel to the San Andreas Fault. The surface-creep signal was expected to range from ~2.5 cm/y north of the town of Parkfield to less than 1 cm/y south of the town of Parkfield (e.g., Titus et al., 2006). Atmospheric delays in the radar images of the interferometric pair could mask this kind of signal in a single interferogram (Zebker et al., 1997; Puysségur et al., 2007). To reduce atmospheric influence on the interferometric phase, we used a methodology widely known as small-baseline subset (SBAS –Berardino et al., 2003). This method was first proposed by Usai et al. (1999) and has been developed in a number of studies (e.g., Lundgren et al., 2001; Usai, 2003; Le Mouelic et al., 2005; Lundgren et al., 2009). Here we used the method as implemented in the GAMMA software as the Multi-Baseline (MB) utility (Wegmüller et al., 2009).

The starting point was a set of 51 single-look complex (SLC) ERS1-2 images that were combined to calculate 341 differential interferograms with a perpendicular baseline of less than 250 meters (Table 1 in the supplementary material). Topographic contributions to the interferometric phase were calculated for each interferogram using the Shuttle Radar Topography Mission (SRTM) 30-m digital elevation model (DEM) and subtracted from the interferograms. The SRTM DEM was also used in a later stage to project the results into a geographic orthoprojection. From the 341 differential interferograms, a subset of 170 high-signal-coherence interferograms was selected based on visual analysis (i.e., signal coherence ≥ ~0.5 on at least ~75% of the dataset). We used the GAMMA Minimum Cost Flow (MCF) algorithm (Costantini and Rosen, 1999; Werner et al., 2002) to unwrap the selected interferograms. For each interferogram, the unwrapping was improved using a phase reference model obtained by unwrapping the multiple-look interferogram. The phase reference model was then resized to the original

pixel resolution. For each pixel, the unwrapped phase value was set to a value which was within the interval (±π) of the model provided and which was consistent with the complex-valued interferogram in the sense that rewrapping of the unwrapped interferogram would result in the original interferogram phase value, except for a constant phase offset (Werner et al., 2002).

Depending on atmospheric conditions, the path delay might have an altitude dependence caused by changes in the atmospheric water vapor and pressure profiles between the acquisitions of the interferometric image pairs (e.g., Doin et al., 2009). In the study region, the atmospheric phase delay is not as exacerbated by extraordinary relief as has been reported elsewhere (e.g., Elliot et al., 2008). To find subtle signals due to land displacements, we used GAMMA to determine the linear regression coefficients of the residual phase with respect to height in the unwrapped interferograms. We used the DEM (in radar geometry) to generate the phase model of the height-dependent atmospheric phase delay for each unwrapped interferogram. Each phase model was then subtracted from the corresponding single interferogram. Then, we applied the MB algorithm.

The MB algorithm uses the weighted least-squares method to generate a time series of unwrapped deformation phases given a multitemporal data stack of unwrapped phases which result primarily from surface deformation. The basic idea is that the total deformation phase at time t_n is the sum of deformations from t_0 to t_1, from t_1 to t_2, …, and from t_{n-1} to t_n (Usai, 2003). The MB-derived time series of the unwrapped deformation phases were used here to derive a time-averaged linear velocity map over the study area (Fig. 2). Then, for each coherent pixel, we calculate a linear regression of the interferometric **phases** with respect to the perpendicular baseline. This procedure revealed unaccounted-for topographic contributions to the interferometric phase (Ferretti et al., 1999), which were then used to improve the linear velocity map. Assuming that potential residual atmospheric contributions behave nonlinearly over time, the linear-velocity map presents a reduced atmospheric contribution (Fig. 2). No *a priori* models of surface displacement were used in any of the processing steps described above.

We concentrate on the near-SAF field (±1.5 km from the fault trace) and we quantify the along-strike spatial variation of the linear surface displacement by taking a number of measurements along the strike. We followed the methodology proposed by Avouac et al. (2006) and Leprince et al. (2007) based on stacked cross-fault profiles (20 profiles for each measurement). Each measurement represents the velocity offset between a cluster of pixels 1.5 km SW of the SAF relative to a cluster of pixels 1.5 km NE of the SAF (Fig. 3).

To highlight possible time-variable creep phenomena, we extracted eleven time series of surface displacements along the SAF from north of the town of Parkfield to south of Highway-46 (located in Fig. 2) at an average distance of ~1.5 km from the SAF trace. The time series (Fig. 4) refer to the fixed Sierra Nevada-Great Valley Block. The time series were filtered over 70 days to remove possible unmodeled residual atmospheric contributions to the interferometric phase. Furthermore, we assigned a color scale to the value of each time series, and each entire series was displayed as a spatiotemporal displacement map (Fig. 5) and associated velocity-changes (Fig 6).

3. Results and discussion

3.1 Spatial distribution of creep

One result of this analysis is the linear displacement rate from 1993 to 2004 measured in the LOS direction of the sensor (23° off the vertical). The bimodal distribution of the surface displacement is consistent with dextral shear (Fig. 2). From ~25 km north of the town of Parkfield to ~15 km south of Gold Hill (Highway 46), the sharp discontinuity in the InSAR signal is a direct consequence of the steady component of surface creep, which is well localized on the SAF. The sharpness of the discontinuity fades progressively from NW to SE along the SAF, possibly indicating that shallow creep to the SE is evolving towards more diffuse (or deeper) displacements.

We assumed that the InSAR signal recorded across the SAF trace is mostly due to horizontal surface displacement. However, there are two main caveats to this assumption. *De facto*, a small amount of normal convergence exists in central California, which is accommodated mainly by contractional structures such as thrust faults and folds in the California Coast Ranges (e.g., Rolandone et al., 2008; Titus et al., 2010). A modest amount of vertical slip may be caused by complex slip distributions near the tips of a creeping fault, similar to the one observed by Bürgmann et al. (1998) at the southern termination of the Hayward fault. An alternative explanation of the InSAR signal is the possible presence of time-dependent groundwater level changes across the SAF that could produce vertical motions, as observed elsewhere on the Hayward fault (Bürgmann, 1998). Unfortunately there is no available water-level records across the SAF along the Parkfield and Cholame sections, therefore we can not document hydrology-related fault vertical slipin this area of the SAF. Known nontectonic subsidence signals are underlined in Fig. 2, they are mainly due to water pumping and gas and oil withdrawal. Subsidence due to water pumping in the Paso Robles Basin, manifested as a bull's-eye-shaped range-change pattern south of the town of Parkfield, is a notable feature of the interseismic interferogram (Fig. 2). Valentine et al. (2001) used ERS InSAR as well as groundwater level data from 58 wells

to study this phenomenon. They did not report that the groundwater level changes reached the Parkfield section of the SAF; this provides confidence that the InSAR signal close to the SAF at Parkfield is primarily tectonic. Similar features, though smaller in area, can be observed in the northern sector of the interseismic interferogram. These correspond to petroleum and gas withdrawal from a shallow reservoir in the Lost Hills field and neighboring reservoirs (Fielding et al., 1998; Brink et al., 2002). Pumping-induced vertical motions are a source of nontectonic signal heterogeneities and are not considered in details in this study.

We compare the along-strike mean-velocity profile (Fig. 3) with available measurements from short-range EDM (Bennett, 1979; Lisowski and Prescott, 1981), creepmeters (Schulz et al., 1982), and alignment array surveys (Burford and Harsh, 1980; Titus et al., 2006) at various locations along the strike on the SAF. According to Lisowski and Prescott (1981), there is no difference between surface creep rates measured using 100-to-200-m-wide alignment arrays and those obtained from the 1-to-2-km-wide short-range EDM located in the same area along the SAF. Therefore, it can be confidently stated that the profile shown in Fig. 3 effectively samples surface creep.

Our creep rates, as measured by InSAR between 1993 and 2004 (Fig 3), are consistent with field measurements along the Parkfield section of the SAF and confirm an overall nearly steady creep rate. Following the 1966 earthquake and its associated afterslip, Lienkaemper and Prescott (1989) observed that the creep rate has been nearly constant on the Parkfield section. Titus et al. (2006) and Rolandone et al. (2008) reported that average surface creep rates had not changed systematically over the last 40 years on the central creeping and Parkfield sections of the SAF. The InSAR observed rates of creep decrease from ~14 mm/y north of the town of Parkfield to zero at about ~12 km south of Highway 46. From this point, and for ~10 km southward, the surface creep rate is approximately zero. It then increases to ~2 mm/y from 22 km southeast of Highway-46 in the in the Cholame section (Fig. 3). This observation is only supported by only one creepmeter measurement by Schulz et al. (1982). The Parkfield area is very well instrumented, but 30 km south of the town

of Parkfield, ground instrumentation is much sparser.

3.2 Comparison with seismicity

Seismicity is not only enhanced on creeping faults, but is also generally highly localized **(e.g. Malservisi et al., 2005)**. In this section, we compare the spatial evolution of surface creep with seismicity catalogs from the Northern California Earthquake Catalog (www.ncedc.org) over the same period of observation as the InSAR data (Fig. 3). We verify that the catalog is consistent for magnitudes equals or greater than 2 and that the relocation accuracy is high enough for the aims of this study. There is a spatial correlation between earthquake locations at depth and the presence of surface creep. The part of the Cholame section with no surface creep also exhibits a gap in seismicity. Apart from few exceptions, in the map view the events on the Parkfield and Cholame sections are well localized on the SAF fault (Fig. 1).

The InSAR measures used here are in good agreement with other estimates of creep rates along the Parkfield section and correlate well with seismicity at depth. In the Cholame section, apparently locked, surface creep that we observe in the southeastern part is also spatially correlated with seismicity. However, seismic slip in the Cholame section has not been reported since the great 1857 Fort Tejón earthquake, and there have been no observations of aseismic slip (e.g., Segall and Harris, 1987; Murray et al., 2001). For instance, Murray and Langbein (2006) used ground-based geodetic data to present a model of slip at depth. Their model shows no resolvable creep between 10 and 30 km south of Gold Hill. Toké and Arrowsmith (2006) reassessed the slip budget along the Parkfield and Cholame sections since 1857. They highlighted the requirement for a change in the interpretation of historically observed fault behavior across the Cholame and in the southeastern portion of the Parkfield sections to balance the SAF slip budget. Based on paleoseismological evidences, Young et al. (2002) can not exclude a post 1857 displacement on this section of the SAF. The creep rate measured in this study (Fig. 3), ~2

mm/yr in the southern portion of the Cholame section and ~5 mm/yr near the northern portion, may change the slip budget of this section of the SAF. If the InSAR-derived aseismic slip in the Cholame section were continuous over time, it would reduce the strain buildup in this section of the SAF by approximately 30 cm from 1857 to 2004, which is an important issue to remember when defining slip budgets **and interpreting geomorphic offsets** (e.g., Sieh, 1978; Lienkaemper, 2001; Zielke et al., 2010). Even though our measurements span **only a decade, we focus on resolving if surface creep** evolves linearly with time (steady creep) or if we are facing episodic aseismic slip.

3.3 Temporal evolution of surface creep

The time series from point 1 to point 11, from NW to SE (Fig. 4), indicates that the temporal evolution of surface creep on the SAF is complex. The time series show periods of episodic creep alternating with periods of steady-state creep resulting in a local creep rate which varies both in time and in space. Time series 1 shows a jump in displacement in 1995, then a three-year period (until 1998) with no displacement, and then a linear increase in displacement until 2004. Time series 2 shows a steady displacement of up to 0.5 mm/y from 1993 to 1994, then a quiet period until 1995, after which the surface creep increased to 0.8 mm/y until 1997. Between 1997 and 1999, time series 2 shows complex surface displacement behavior. From 1999 to 2004, the surface displacement increased almost linearly with time. Time series 3 shows a steady displacement between 1993 and mid-2002 and almost no displacement since then. Time series 4 is located ~2 km from the 2004 Parkfield earthquake epicenter. **The collective time series data does not show evidence for anomalous creep behavior prior to the** 2004 Parkfield earthquake or related to the M6.5 December 2003 San Simeon earthquake 50 km west (e.g., Rolandone et al., 2006); even though the San Simeon event increased the shear stress on the Parkfield section (Johanson and Bürgmann, 2010).

The USGS maintains a creepmeter network in the field, for which the data are available (http://earthquake.usgs.gov/monitoring/deformation/data/). **Time series points 1-4 from**

this study lie close to USGS creepmeters. **For these sites** we compare time series of the creepmeters values with our InSAR time series for the period 1993 to 2004 (Fig. 4). For time series 1 to 3, the InSAR time series follow the general trend depicted by the creepmeters time series, except for some high-frequency discrepancies. Time series 4 and the creepmeter at Gold Hill show a similar trend from 1993 to late 1999. After 1999, the InSAR data recorded an increase in creep activity in this section of the San Andreas Fault that was not recorded by the creepmeter at Gold Hill. Because the InSAR values are taken ~1.5 km apart across the fault trace while the Gold Hill creepmeter is only 10 meters-long wire baseline (John Langbein, pers. comm.), we suggest that the creepmeter at Gold Hill resides on a momentarily inactive branch of the San Andreas Fault. This result confirms the observations of Titus at al. (2006) and Toké et al. (2011) that along the Parkfield section, significant slip may be accommodated by structures in a wider SAF zone. This observation highlights how InSAR complements more traditional methods of observation and could be used to plan field instrumentation.

The lack of dense temporal data coverage hampers a detailed comparison between our results obtained by InSAR and those obtained by Murray and Segall (2005). Using time-dependent slip inversions of two-color EDM data, Murray and Segall (2005) found that a slip-rate increase occurred between January 1993 and July 1996 on the upper 8 km of the fault near Middle Mountain. The slip-rate evolution appeared to be episodic, with an initial modest increase after an October 1992 M4.3 earthquake and a much larger jump following a shallower M4.7 event in December 1994. They concluded that the temporal correlation between inferred slip and seismicity suggests that moderate earthquakes triggered the aseismic fault slip. Unfortunately, ERS InSAR data are not available between the end of 1993 and the beginning of 1995, and in time series 1 and 2, the jump in the data of 1 cm in the LOS, which is equivalent to a horizontal displacement of 3.3 cm, occurs between periods of no displacement. At the end of the Parkfield section, time series 5 also exhibits the first jump and then another rapid increase since 2002. Time series 6 to 11 also exhibit periods of episodic creep, but with smaller magnitudes. In time series 6, most of the displacement occurred before 1996, whereas three periods of rapid displacement are evident in time series 7. In time series 9 and 10, an increase in displacement between mid-1997 and the end of 1999 separates periods with almost

no displacement. Time series11 exhibits surface displacement only after 2003. These observations show that there is a time variable surface creep in the Cholame section of the SAF.

3.4 Spatiotemporal observations

Nadeau and McEvilly (1999, 2004) noted that seismicity at depth follows and is driven by deep fault creep. We compare our InSAR results with microseismicity to investigate first order microseismicity changes with variations in surface spatiotemporal creep evolution. We show the spatiotemporal evolution of surface creep from InSAR data (Fig. 5) and its velocity changes (Fig. 6). We compare them to the spatiotemporal distribution of earthquakes (and their magnitude) from northwest of the town of Parkfield to south east of Highway-46 (A-A' in figure 1). The first derivative of the spatiotemporal evolution of surface creep (Fig. 6) highlights local changes in the slope of the time series representing local changes in creep rates (acceleration or deceleration). Pulses of surface displacement in Figure 6 correspond to episodic creep at the surface.

Four remarkable features stand out from the **spatio-temporal analysis (Figures 5-6)**. First, surface creep evolves nonlinearly both in space and in time. Second, surface creep occurs where seismic activity occurs at depth. There is a seismicity gap around 120.16°W longitude, ~18 km SE of Highway 46, where cumulative surface creep is minimal (as is also highlighted in Fig. 3). Third, cumulative surface creep seems to be more pronounced where seismic activity is higher at depth. Last, the Cholame segment of the SAF not only experiences episodic creep at the surface, but also manifests seismic activity at depth (as also reported by Waldhauser and Schaff, 2008).

4. Conclusions

The Parkfield and the Cholame sections of the SAF experienced both temporally and spatially variable surface creep between 1993 and 2004. Both episodic creep and

periods of steady-state aseismic slip were observed using InSAR data (Fig. 4). The onset of surface creep is variable in time and space along these sections of the SAF (Fig. 5), leading to localized creep acceleration or pulses of surface displacement (Fig. 6). Although seismic activity at depth is well correlated in space with creep activity at the surface, the InSAR data used in this research do not enable a robust investigation of first-order time-dependent relationships between seismic moment released at depth and triggering of episodic creep at the surface.

The spatial pattern of the interseismic displacement rate (Fig. 2) indicates that tectonic strain was not uniformly distributed along the strike of the fault between 1993 and 2004. **Similarly to other geodetic techniques,** we observe a decrease in the creep rate from Parkfield, **CA** to **just southeast** of Highway 46 (1.4 ±0.3 cm/yr to 0.06 ±0.3 cm/yr). **However, this study shows evidence for episodic creep further southeast** on the Cholame section **of the SAF (up to** 0.2 ±0.1 cm/yr, Fig. 3). The evidence of episodic creep in the Cholame section of the SAF ~45 km south of the town of Parkfield is in contrast with previous interpretations of GPS and trilateration data (e.g., by Murray and Segall, 2005). Paleoseismic studies of the Cholame section of the SAF (Stone et al. 2002; Young at al., 2002) could not rule out the possibility of a post-1857 displacement. In fact, post-1857 fracturing **was** observed at the Las Yeguas site (Young et al., 2002). Our InSAR results support the need for close monitoring of the Cholame section of the SAF where the 1857 Fort Tejón earthquake **likely** nucleated (**e.g., Sieh, 1978**) and where recent evidence of deep slow slip were revealed by tremors (Shelly et al., 2009).

Acknowledgements

The authors are thankful to Roland Bürgmann for valuable discussions and comments on this work. Comments by two anonymous reviewers greatly improved the manuscript. BRGM Research Direction also supported this work. We thank the European Space Agency (ESA) for providing ERS1-2 data in the framework of the Category-1 research proposal. We are also grateful to the California Geological Survey for providing the

1 original issue of *California Geology*, v. 32 (1979).

5. References

Akçiz, S.O., Ludwig, L.G., Arrowsmith, J.R., Zielke, O., 2010. Century-long average time intervals between earthquake ruptures of the San Andreas Fault in the Carrizo Plain. *California Geology*, 38(9), 787–790.

Avouac, J.-P., Ayoub, F., Leprince, S., Konca, O., Helmberger, D.V., 2006. The 2005, M_w 7.6 Kashmir earthquake: subpixel correlation of 3 ASTER images and seismic waveform analysis. *Earth and Planetary Science Letters* 249(3–4), 514–528.

Bakun, W.H., McEvilly, T.V., 1984. Recurrence models and the Parkfield, California earthquake. *J. Geophys. Res.* 89(B5), 3051–3058.

Bakun, W.H., Aagaard, B., Dost, B., Ellsworth, W.L., Hardebeck, J.L., Harris, R.A., Ji, C., Johnston, M.J.S., Langbein, J., Lienkaemper, J.J., Michael, A.J., Murray, J.R., Nadeau, R.M., Reasenberg, P.A., Reichle, M.S., Roeloffs, E.A., Shakal, A., Simpson, R.W., Waldhauser, F., 2005. Implications for prediction and hazard assessment from the 2004 Parkfield earthquake. *Nature* 437, 969–974.

Bennett J. H., 1979. Fault creep measurements. *California Geology* 32(5), 98–105.

Berardino, P., Fornaro, G., Lanari, R., Sansosti, E., 2002. A new algorithm for surface deformation monitoring based on small baseline differential SAR interferograms. *IEEE Transactions on Geoscience and Remote Sensing* 40, 2375–2383.

Brink, J.L., Patzek, T.W., Silin, D.B., Fielding, E.J., 2002. Lost Hills field trial—incorporating new technology for reservoir management. Paper presented at the SPE Annual Technical Conference and Exhibition, San Antonio TX, September 29–October 2, 2002. Available at http://petroleum.berkeley.edu/papers/patzek/spe77646.pdf.

Burford, R.O., Harsh, P.W., 1980. Slip on the San Andreas Fault in central California

from alignment array surveys. *Bull. Seismol. Soc. Am.* 70(4), 1233–1261.

Bürgmann, R., Fielding E.J., Sukhatme, J., 1998. Slip along the Hayward Fault, California, estimated from space-based synthetic aperture radar interferometry. *Geology* 26, 559–562.

Costantini, M., Rosen, P.A., 1999. A generalized phase unwrapping approach for sparse data. *Proceedings, IGARSS '99*, Hamburg, Germany, June 28–July 2, 267–269.

DeMets, C., Gordon, R.G., Argus, D.F., Stein, S., 1994. Effect of recent revisions to the geomagnetic reversal time scale on estimates of current plate motions. *Geophys. Res. Lett.* 21, 2191–2194.

Doin, M.-P., Lasserre, C., Peltzer, G., Cavalié, O., Doubre, C., 2009. Corrections of stratified tropospheric delays in SAR interferometry: validation with global atmospheric models. Journal of Applied Geophysics 69(1), 35–50.

Elliot, J.R., Biggs, J., Parsons, B., Wright, T.J., 2008. InSAR slip rate determination on the Altyn Tagh Fault, northern Tibet, in the presence of topographically correlated atmospheric delays. *Geophys. Res. Lett.* 35, L12309 doi:10.1029/2008GL033659.

Farr, T.G., Caro, E., Crippen, R., Duren, R., Hensley, S., Kobrick, M., Paller, M., Rodriguez, E., Rosen, P., Roth, L., Seal, D., Shaffer, S., Shimada, J., Umland, J., Werner, M., Oskin, M., Burbank, D., Alsdorf, D., 2004. The shuttle radar topography mission. *Reviews of Geophysics* 45, doi: 1029/2005RG000183.

Ferretti, A., Prati, C., Rocca, F., 1999. Permanent scatterers in SAR interferometry. *Proceedings, Geoscience and Remote Sensing Symposium*, June 28–July 2, 1999, Hamburg, Germany, 1528–1530.

Fialko, Y., 2006. Inter-seismic strain accumulation and the earthquake potential on the

southern San Andreas Fault system. *Nature* 44, 968–971.

Fielding, E.J., Bloom, R.G., Goldstain, R.M., 1998. Rapid subsidence over oil fields measured by SAR interferometry. *Geophys. Res. Lett.* 25, 3215–3218.

Gao, S.S., Silver, P.G., Linde, A.T., 2000. Analysis of deformation data at Parkfield, California: detection of a long-term strain transient. *J. Geophys. Res.* 105, 2955–2967.

Johanson, I.A., Bürgmann, R., 2005. Creep and quakes on the northern transition zone of the San Andreas Fault from GPS and InSAR data. *Geophys. Res. Lett.* 32, L14306, doi:10.1029/2005GL023150.

Johanson, I.A., Fielding, E.J., Rolandone, F., Bürgmann, R., 2006. Coseismic and postseismic slip of the 2004 Parkfield earthquake from space geodetic data. *Bull. Seismol. Soc. Am.* 96(4B), S269–S282.

Johanson, I.A., Bürgmann, R., 2010. Coseismic and postseismic slip from the 2003 San Simeon earthquake and their effects on backthrust slip and the 2004 Parkfield earthquake. *J. Geophys. Res.* 115, B07411, doi:10.1029/2009JB006599.

Langbein, J., Gwyther, R.L., Hart, R.H.G., Gladwin, M.T., 1999. Slip-rate increase at Parkfield in 1993 detected by high-precision EDM and borehole tensor strainmeters. *Geophys. Res. Lett.* 26(16), 2529–2532.

Le Mouélic, S., Raucoules, D., Carnec, C., King, C., 2005. A least-squares adjustment of multi-temporal InSAR data: application to the ground deformation of Paris. *Photogram. Eng. Rem. S.* 71, 197–204.

Leprince, S., Barbot, S., Ayoub, F., Avouac, J.-P., 2007. Automatic and precise orthorectification, coregistration, and subpixel correlation of satellite images: application to ground deformation measurements. *IEEE Trans. Geosci. Remote Sens.* 45, 1529–

1558.

Lienkaemper, J.J., Prescott, W.H., 1989. Historic surface slip along the San Andreas Fault near Parkfield, California. *J. Geophys. Res.* 94(B12), 17, 647–670, doi:10.1029/JB094iB12p17647.

Lienkaemper, J.J., 2001. 1857 slip on the San Andreas Fault Southeast of Cholame, California. *Bull. Seismol. Soc. Am.* 91(6), 1659–1672.

Lisowski, M., Prescott, W.H., 1981. Short-range distance measurements along the San Andreas Fault system in central California, 1975 to 1979. *Bull. Seismol. Soc. Am.* 71(5), 1607–1624.

Lyon, S., Sandwell, D., 2003. Fault creep along the southern San Andreas from interferometric synthetic aperture radar, permanent scatterers, and stacking. *J. Geophys Res.* 108(B1), 2047, doi:10.1029/2002JB001831.

Lundgren, P., Usai, S., Sansosti, E., Lanari, R., Tesauro, M., Fornaro, G., Berardino, P., 2001. Modeling surface deformation observed with synthetic aperture radar interferometry at Campi Flegrei caldera. *J. Geophys. Res.* 106(19), 355-366, doi:10.1029/2001JB000194.

Lundgren, P., Hetland, E.A., Liu, Z., Fielding, E.J., 2009. Southern San Andreas-San Jacinto Fault system slip rates estimated from earthquake cycle models constrained by GPS and interferometric synthetic aperture radar observations. *J. Geophys. Res.* 114, B02403, doi:10.1029/2008JB005996.

Malservisi, R., Furlong, K. P., Gans, C. R., 2005. Microseismicity and creeping faults: Hints from modeling the Hayward fault, California (USA), Earth and Planetary Science Letters, 234 (3-4), 421-435.

Massonnet, D., Feigl, K.L., 1998. Radar interferometry and its application to changes in the earth's surface. *Rev. Geophys.* 36, 441–500.

McEvilly, T.V., Bakun, W.H., Casaday, K.B., 1967. The Parkfield, California earthquake of 1966. *Bull. Seismol. Soc. Am.* 57(6), 1221–1244.

Murray, J.R., Segall, P., 2005. Spatiotemporal evolution of a slip-rate increase on the San Andreas Fault near Parkfield, California. *J. Geophys. Res.* 110, B09407, doi:10.1029/2005JB003651.

Murray, J., Langbein, J., 2006. Slip on the San Andreas Fault at Parkfield, California, over two earthquake cycles and the implications for seismic hazard. *Bull. Seismol. Soc. Am.* 96, 283–303.

Nadeau, R.M., McEvilly, T.V. 1999. Fault slip rates at depth from recurrence intervals of repeating microearthquakes. *Science* 285(5428), 718–721.

Nadeau, R.M., McEvilly, T.V., 2004. Periodic pulsing of characteristic microearthquakes on the San Andreas Fault. *Science* 303(5655), 220–222.

Puysségur, B., Michel, R., Avouac, J.-P., 2007. Tropospheric phase delay in interferometric synthetic aperture radar estimated from meteorological model and multispectral imagery. *J. Geophys. Res.* 112, B05419 doi:10.1029/2006JB004352.

Roeloffs, E., Langbein, J., 1994. The earthquake prediction experiment at Parkfield, California. *Rev. Geophys.* 32, 315–336.

Rolandone, F., Dreger, D., Murray, M., Bürgmann, R., 2006. Coseismic slip distribution of the 2003 M_w 6.6 San Simeon earthquake, California, determined from GPS measurements and seismic waveform data. *Geophys. Res. Lett.* 33, L16315, doi:10.1029/2006GL027079.

Rolandone, F., Bürgmann, R., Agnew, D.C., Johanson, I.A., Templeton, D.C., d'Alessio, M.A., Titus, S.J., DeMets, C., Tikoff, B., 2008. Aseismic slip and fault normal strain along the central creeping section of the San Andreas Fault. *Geophys. Res. Lett.* 35, L14305, doi:10.1029/ 2008GL034437.

Rosen, P., Werner, C., Fielding, E., Hensley, S., Buckley, S., Vincent, P., 1998. Aseismic creep along the San Andreas Fault northwest of Parkfield, CA measured by radar interferometry. *Geophys. Res. Lett.* 25, 825–828.

Scharer, K.M., Biasi, G.P., Weldon, R.J. II, Fumal, T.E., 2010. Quasi-periodic recurrence of large earthquakes on the southern San Andreas Fault. *Geology* 38, 555–558.

Shelly, D.R., Ellsworth, W.L., Ryberg, T., Haberland, C., Fuis, G.S., Murphy, J., Nadeau, R.M., Bürgmann, R., 2009. Precise location of San Andreas Fault tremors near Cholame, California, using a seismometer cluster: slip on the deep extension of the fault? *Geophys. Res. Lett.* 36, L01313, doi:10.1029/2008GL036367.

Schulz, S.S., Mavko, G.M., Burford, R.O., Stuart, W.D., 1982. Long-term fault creep observations in central California. *J. Geophys. Res.* 87(B8), 6977–6982.

Sieh, K.E., 1978. Slip along the San Andreas Fault associated with the great 1857 earthquake. *Bull. Seismol. Soc. Am.* 68(5), 1421–1448.

Sieh, K.E., Jahns, R.H., 1984. Holocene activity of the San Andreas Fault at Wallace Creek, California. *Geol. Soc. Am. Bull.* 95, 883–896.

Stone, E.M., Grant, L.B., Arrowsmith, J.R., 2002. Recent rupture history of the San Andreas Fault southeast of Cholame in the Northern Carrizo Plain, California. *Bull. Seismol. Soc. Am.* 92(3), 983–997.

Titus, S.J., De Mets, C., Tikoff, B., 2006. Thirty-five-year creep rates for the creeping segment of the San Andreas Fault and the effects of the 2004 Parkfield earthquake: constraints from alignment arrays, continuous global positioning systems, and creepmeters. *Bull. Seismol. Soc. Am.* 96, 250–268.

Titus, S., Dyson, M., DeMets, C., Tikoff, B., Rolandone, F., Bürgmann, R., 2011. Geologic versus geodetic deformation adjacent to the San Andreas Fault, central California. *Geological Society of America Bulletin*, doi:10.1130/B30150.1.

Toké, N.A., Arrowsmith, J.R., 2006. Reassessment of a slip budget along the Parkfield segment of the San Andreas Fault. *Bull. Seismol. Soc. Am.* 96, 339–348.

Toké, A.N., Arrowsmith, J.R., Rymer, M.J., Landgraf, A., Haddad, D.E., Busch, M., Coyan J., Hannah, A., 2011. Late Holocene slip rate of the San Andreas Fault and its accommodation by creep and moderate-magnitude earthquakes at Parkfield, California. *Geology* 39(3), 243–246, doi:10.1130/G31498.1.

Usai, S., Delgaudio, C., Borgstrom, S., Achilli, D., 1999. Monitoring terrain deformations at Phlegrean Fields with SAR interferometry. *Proceedings, 2nd International Workshop on SAR Interferometry (FRINGE99)*, European Space Agency, Liege, Belgium, unpaginated CD-ROM.

Usai, S., 2003. A least-squares database approach for SAR interferometric data. *IEEE Transactions on Geoscience and Remote Sensing* 41, 753–760.

U.S. Geological Survey and California Geological Survey, 2006. Quaternary fault and fold database for the United States. Accessed 2009 from USGS web site: http://earthquakes.usgs.gov/regional/qfaults/ .

Valentine, D.W., Densmore, J.N., Galloway, D.L., Amelung, F., 2001. Use of InSAR to identify land-surface displacement caused by aquifer-system compaction in the Paso

Robles area, San Luis Obispo County, California, March to August 1997. *USGS Open File Rept. 00-447*.

Waldhauser, F., Schaff, D.P., 2008. Large-scale relocation of two decades of Northern California seismicity using cross-correlation and double-differencing methods. *J. Geophys. Res.* 113, B08311, doi:10.1029/2007JB005479.

Wegmüller, U., Werner, C.L., 1997. GAMMA SAR processor and interferometry software. *Proceedings, 3rd ERS Scientific Symposium,* Florence, Italy, March 17–20.

Wegmüller, U., Werner, C.L., Santoro, M., 2009. Motion monitoring for Etna using ALOS PALSAR time series. *Proceedings, ALOS PI Symposium 2009*, November 9–13, Hawaii.

Weldon, R.J., Fumal, T.E., Biasi, G.P., Scharer, K.M., 2005. Geophysics—past and future earthquakes on the San Andreas Fault. *Science* 308, 966–967.

Werner, C., Wegmüller, U., Strozzi, T., 2002. Processing strategies for phase unwrapping for InSAR applications. *Proceedings, EUSAR Conference*, June 4–6, Cologne, Germany, unpaginated CD-ROM.

Whitten, C.A., Claire, C.N., 1960. Creep on the San Andreas Fault: analysis of geodetic measurements along the San Andreas Fault. *Bull. Seismol. Soc. Am.* 50(6), 404–415.

Young, J.J., Arrowsmith, J.R., Colini, L., Grant, L.B., Gootee, B., 2002. Three-dimensional excavation and recent rupture history along the Cholame segment of the San Andreas Fault. *Bull. Seismol. Soc. Am.* 92(7), 2670–2688.

Zebker, H.A., Rosen, P.A., Hansley, H., 1997. Atmospheric effects in interferometric synthetic aperture radar surface deformation and topographic maps. *J. Geophys. Res.* 102, 7547–7563.

Zielke, O., Arrowsmith, J.R., Ludwig, L.G., Akçiz, O.S., 2010. Slip in the 1857 and earlier large earthquakes along the Carrizo plain, San Andreas Fault. *Science* 327(2), 1119–1122, doi: 10.1126/science.1182781.

Figure Captions.

Figure 1. Map of the Parkfield region of the SAF showing the location of major Quaternary faults (red lines; USGS fault map, 2006). SAF: San Andreas Fault, RC: Rinconada Fault, SJ: San Juan Fault, LP: La Panza Fault, and SC: South Cuyama Fault. H-46 stands for Highway 46. SAFOD stands for San Andreas Fault Observatory at Depth. The epicenters and USGS moment tensors (http://earthquake.usgs.gov) of the 1966 and 2004 earthquakes are indicated. Creeping Parkfield and Cholame sections are drawn following Toké and Arrowsmith (2006). The black dotted line represents the ground swath shared by the ERS1-2 radar scenes. Blue dots represent seismicity at depth between 1993 and 2004, limited to within A-A' in the radar scene and limited to within plus-minus 10 km across the SAF. Gray arrows indicate important sites along the Parkfield and Cholame sections of the SAF and the approximate trenching location **following** Stone et al. (2002) and Toke et al. (2011). Topography is from the Shuttle Radar Topography Mission (SRTM) (Farr et al., 2004) digital elevation model.

Figure 2. Linear surface displacement rate in the LOS direction of the satellite (23° off the vertical) between 1993 and 2004. Negative values represent surface displacement away from the satellite due to westward motion (or land subsidence). The deformation field reflects creep and interseismic strain buildup on the SAF in the Parkfield area before the 2004 earthquake. 2004 and 1966 earthquake epicenters (white stars) are plotted, as well as USGS moment tensors (http://earthquake.usgs.gov). Locations 1-11 (numbered circles) are where the time series of surface displacements along the SAF were measured (Fig. 4). Nontectonic subsidence features are also highlighted: Coalinga (CO), Lost Hills (LH), Kettleman North Dome oilfield-related subsidence (KND), and Paso Robles Basin subsidence (PR) due to groundwater level changes. PKF stands for the town of Parkfield (CA), GH for Gold Hill.

Figure 3. Top: Profile showing the linear surface slip rate along the strike of the SAF (A-A' in Fig. 1) from north west of Parkfield CA to south east of Highway-46 (longitude 120°W) between 1993 and 2004 from InSAR data (values are in cm/y, projected horizontally, parallel to the fault strike, right lateral positive). InSAR values are compared with historical records from EDM, alignment arrays, and creepmeters (**plotted with error bars**). Red stars show the location of 1966 and 2004 Parkfield earthquakes. Bottom: seismicity (1993–2004) within plus-minus 10 km of the SAF plotted as longitude versus depth (source: Northern California Earthquake Data Center).

Figure 4. Time series of surface displacements extracted at locations 1 to 11 (Fig. 2) irregularly sampled approximately every ~8 km. These time series show the temporal evolution of surface displacement measured within ±1.5 km perpendicular to the main trace of the SAF. Values are in meters, projected horizontally, parallel to the fault strike. Orange dots represent in situ creepmeters values at location 1 to 4 (source USGS) spanning 1993-2004. 1- Middle Ridge creepmeter; 2- Varian Ranch creepmeter; 3- Parkfield creepmeter; 4- Gold Hill creepmeter.

Figure 5. Map view of the spatiotemporal evolution of cumulative surface creep on the SAF from north west of the town of Parkfield to south east of Highway-46, plotted against seismicity. Displacement values are given in the line-of-sight direction (LOS is 23° off the vertical). Numbers 1 to 11 represent time series location (Fig. 2). White spaces indicate **periods with no data**. Pixel spacing resulting from spatial interpolation of the time series is ~4 km. The average time between two temporal samples is 2.75 months. H-46 indicates the approximate position of Highway-46. The approximate epicenter positions of the 1966 and 2004 Parkfield earthquakes are also shown.

Figure 6. Map view of the spatiotemporal velocity changes of surface creep on the SAF from north of the town of Parkfield to south east of Highway-46, plotted against

seismicity. Displacement values are given in the line-of-sight direction (LOS is 23° off the vertical). Numbers 1 to 11 represent time series locations (Fig. 2). White spaces indicate **periods with no data**. Pixel spacing resulting from spatial interpolation of the time series (*y*-direction) is ~4 km. The average time between two temporal samples (*x*-direction) is 2.75 months. H-46 is the approximate position of Highway 46. Approximate epicenter positions of the 1966 and 2004 Parkfield earthquakes are also shown.

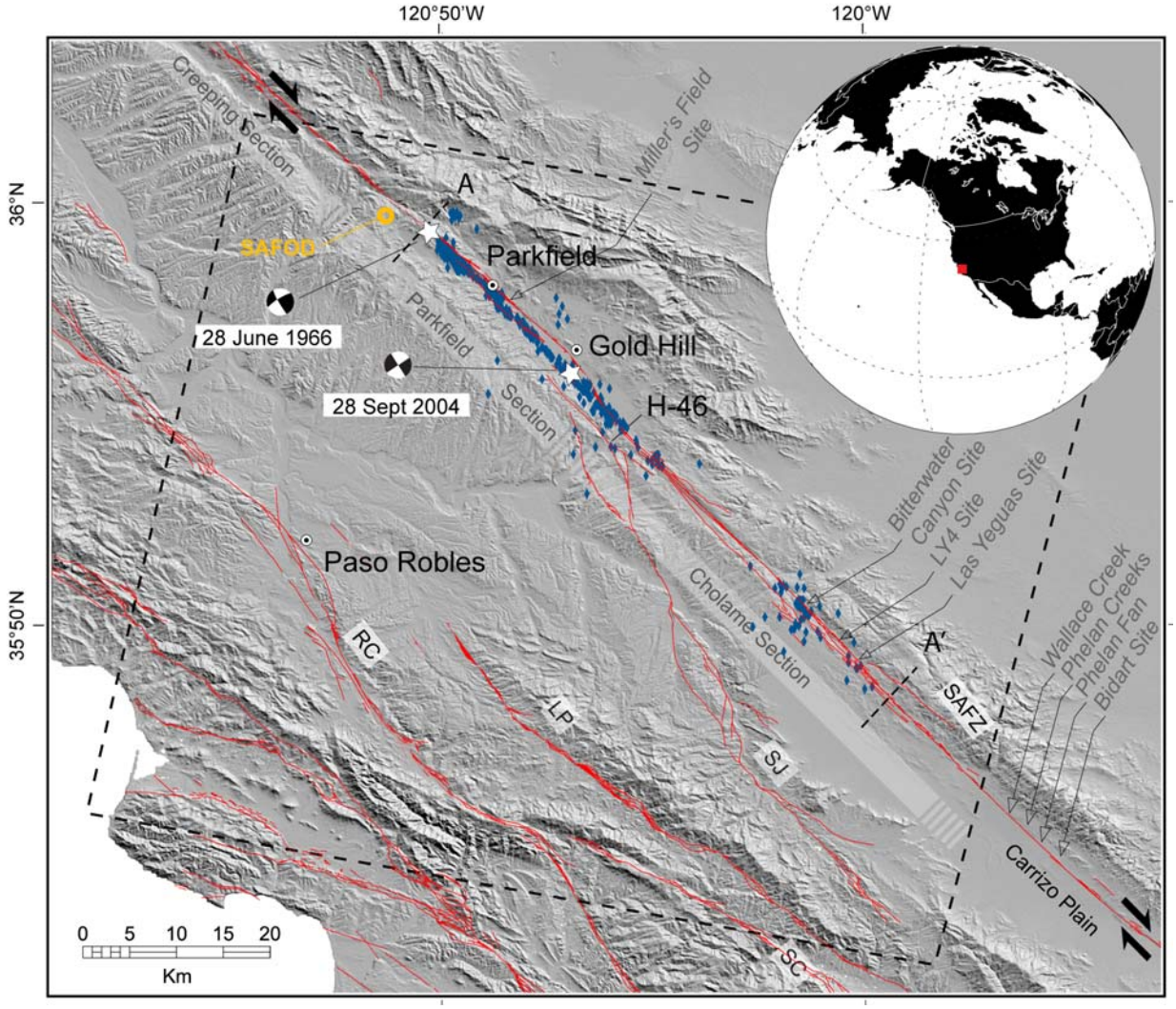
120°50'W
120°W
36°N
35°50'N
Creeping Section
Miller's Field Site
A
SAFOD
Parkfield
28 June 1966
Parkfield Section
Gold Hill
28 Sept 2004
H-46
Bitterwater
Canyon Site
LY4 Site
Las Yeguas Site
Paso Robles
Cholame Section
A'
Wallace Creek
Phelan Creeks
Phelan Fan
Bidart Site
RC
LP
SJ
SAFZ
Carrizo Plain
SC
0 5 10 15 20
Km

FIG 1

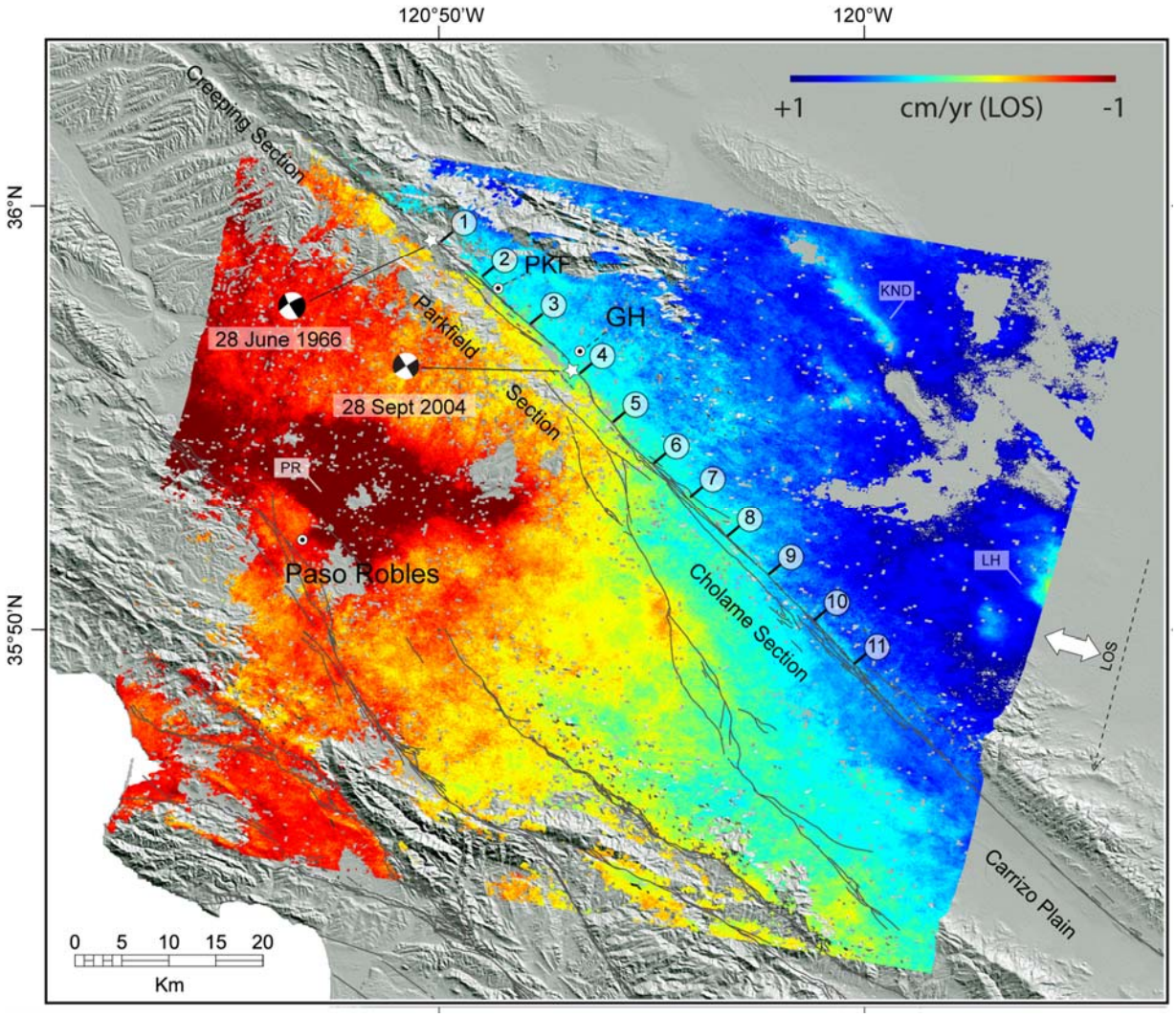
120°50'W
120°W
36°N
35°50'N
+1
cm/yr (LOS)
-1
Creeping Section
Parkfield
Section
Cholame Section
28 June 1966
28 Sept 2004
PKF
GH
KND
LH
PR
Paso Robles
Carrizo Plain
LOS
1
2
3
4
5
6
7
8
9
10
11
0 5 10 15 20
Km

FIG 2

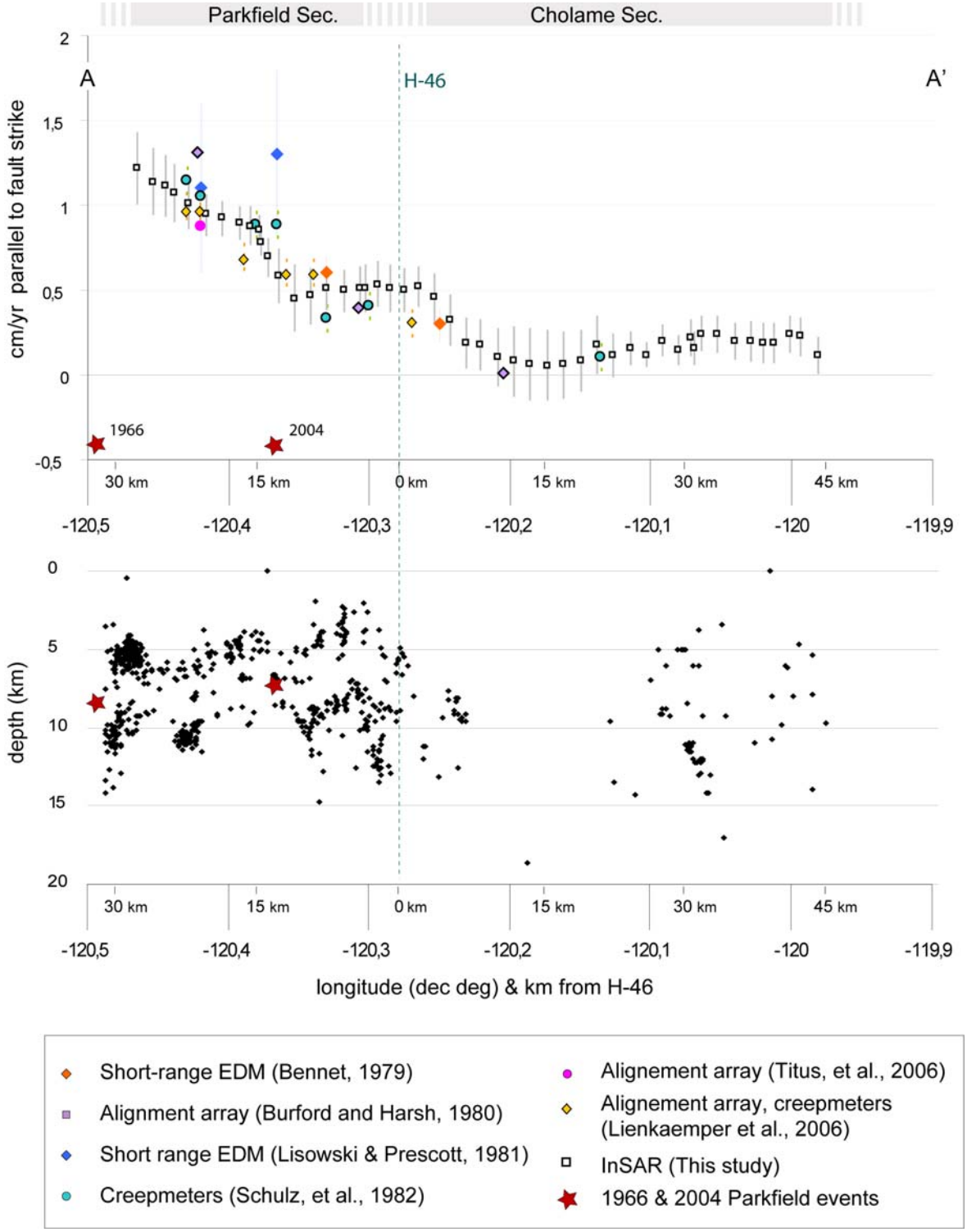
Parkfield Sec.
Cholame Sec.
A
H-46
A'
cm/yr parallel to fault strike
2
1,5
1
0,5
0
-0,5
1966
2004
30 km
15 km
0 km
15 km
30 km
45 km
-120,5
-120,4
-120,3
-120,2
-120,1
-120
-119,9
depth (km)
0
5
10
15
20
longitude (dec deg) & km from H-46
Short-range EDM (Bennet, 1979)
Alignment array (Burford and Harsh, 1980)
Short range EDM (Lisowski & Prescott, 1981)
Creepmeters (Schulz, et al., 1982)
Alignement array (Titus, et al., 2006)
Alignement array, creepmeters (Lienkaemper et al., 2006)
InSAR (This study)
1966 & 2004 Parkfield events

FIG 3

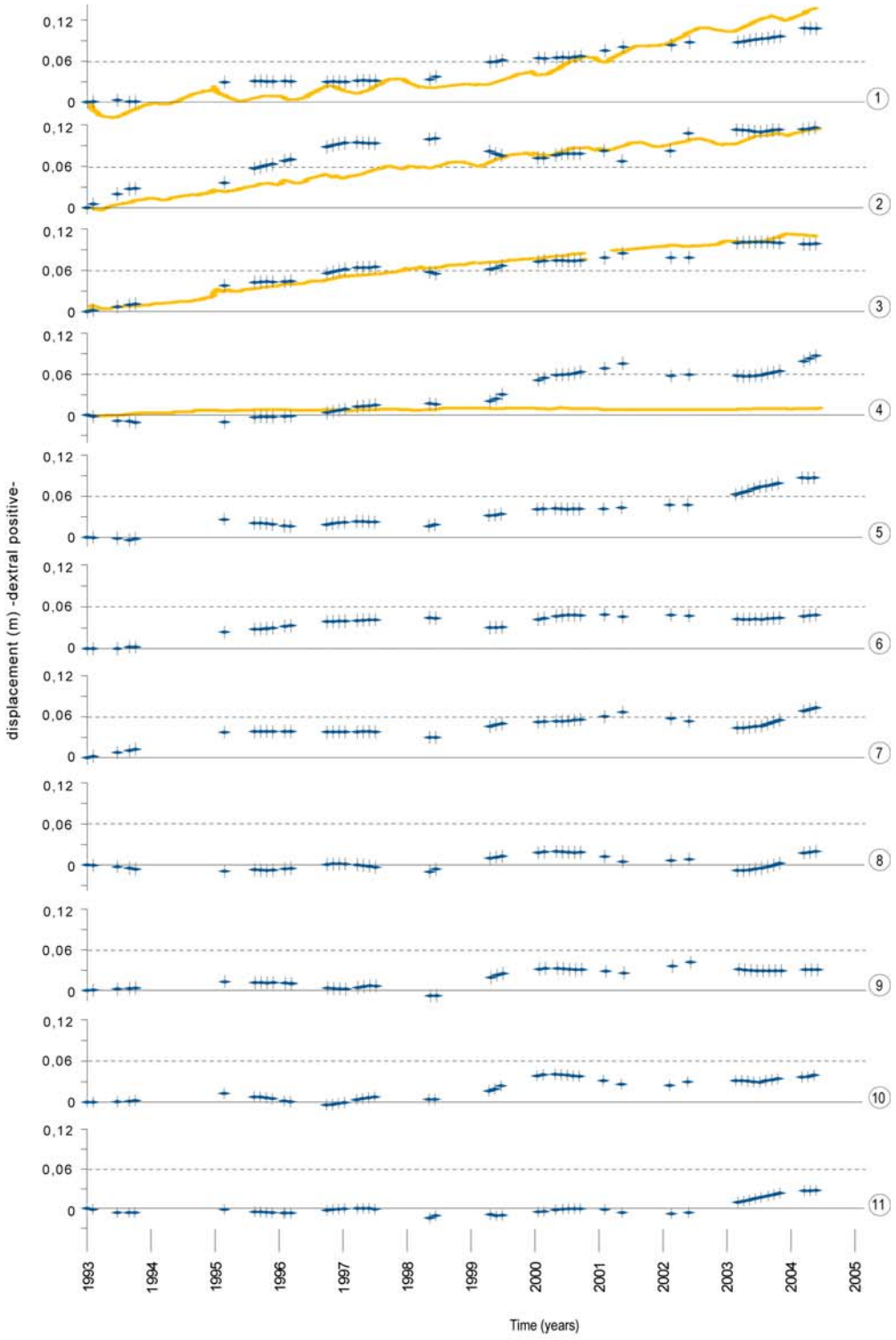
displacement (m) -dextral positive-
0,12
0,06
0
1
2
3
4
5
6
7
8
9
10
11
1993
1994
1995
1996
1997
1998
1999
2000
2001
2002
2003
2004
2005
Time (years)

1 FIG 4

1

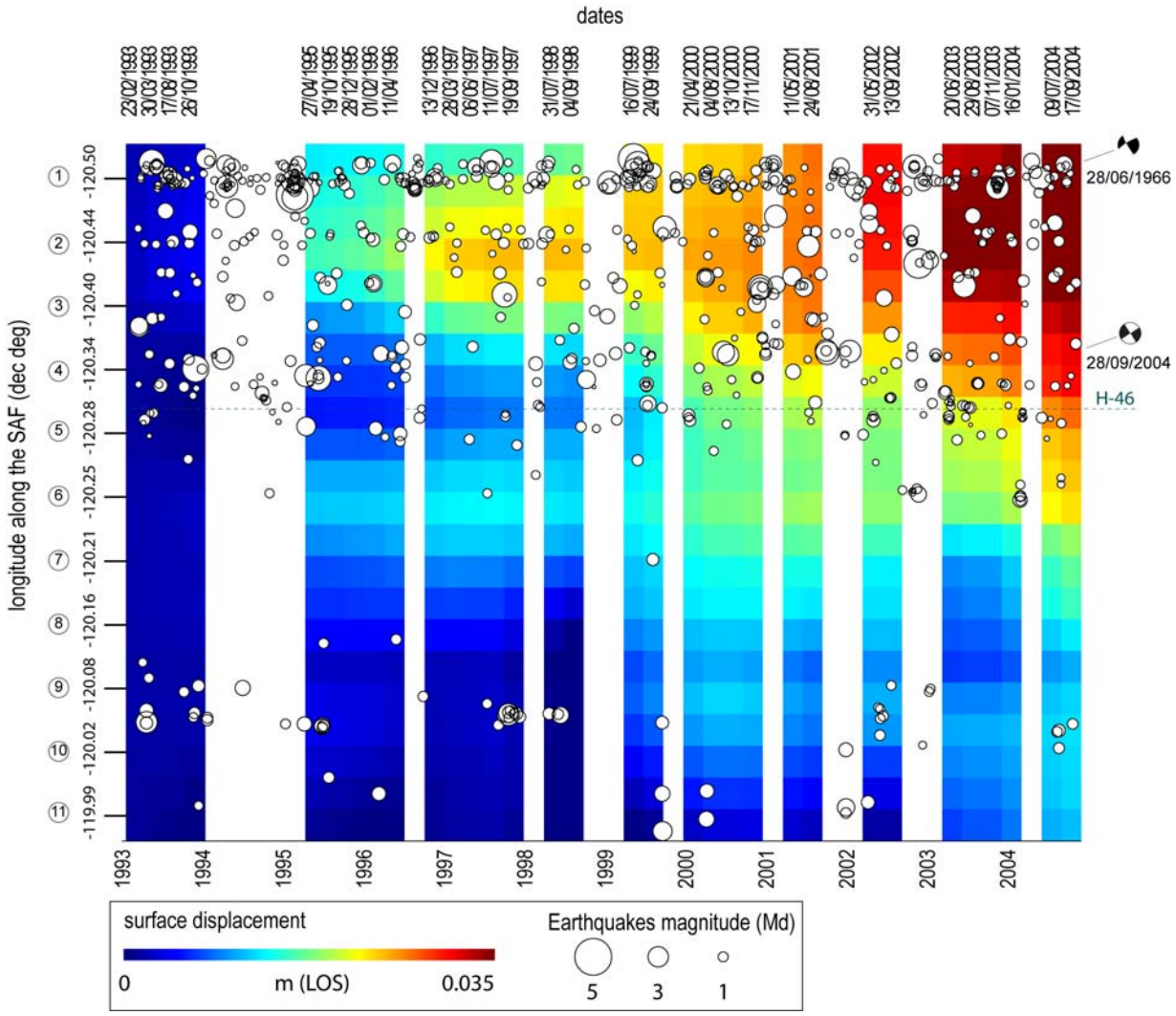
dates
23/02/1993
30/03/1993
17/08/1993
26/10/1993
27/04/1995
19/10/1995
28/12/1995
01/02/1996
11/04/1996
13/12/1996
28/03/1997
06/06/1997
11/07/1997
19/09/1997
31/07/1998
04/09/1998
16/07/1999
24/09/1999
21/04/2000
04/08/2000
13/10/2000
17/11/2000
11/05/2001
24/08/2001
31/05/2002
13/09/2002
20/05/2003
29/08/2003
07/11/2003
16/01/2004
09/07/2004
17/09/2004
longitude along the SAF (dec deg)
1 -120.50
2 -120.44
3 -120.40
4 -120.34
5 -120.28
6 -120.25
7 -120.21
8 -120.16
9 -120.08
10 -120.02
11 -119.99
1993
1994
1995
1996
1997
1998
1999
2000
2001
2002
2003
2004
28/06/1966
28/09/2004
H-46
surface displacement
0
m (LOS)
0.035
Earthquakes magnitude (Md)
5
3
1

FIG 5

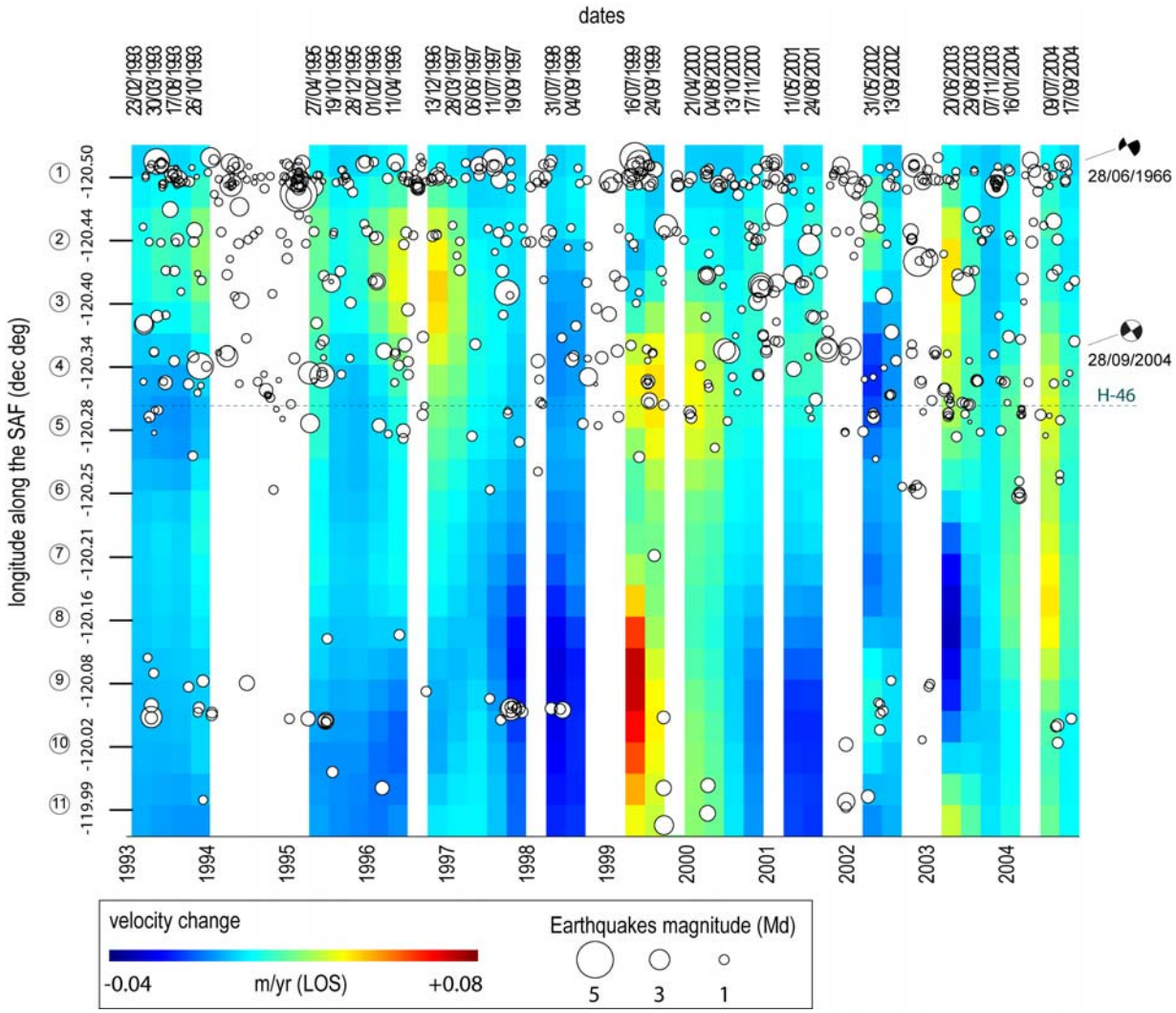
dates
23/02/1993
30/03/1993
17/08/1993
26/10/1993
27/04/1995
19/10/1995
28/12/1995
01/02/1996
11/04/1996
13/12/1996
28/03/1997
06/06/1997
11/07/1997
19/09/1997
31/07/1998
04/09/1998
16/07/1999
24/09/1999
21/04/2000
04/09/2000
13/10/2000
17/11/2000
11/05/2001
24/08/2001
31/05/2002
13/09/2002
20/06/2003
29/08/2003
07/11/2003
16/01/2004
09/07/2004
17/09/2004
longitude along the SAF (dec deg)
1 -120.50
2 -120.44
3 -120.40
4 -120.34
5 -120.28
6 -120.25
7 -120.21
8 -120.16
9 -120.08
10 -120.02
11 -119.99
1993
1994
1995
1996
1997
1998
1999
2000
2001
2002
2003
2004
28/06/1966
28/09/2004
H-46
velocity change
-0.04
m/yr (LOS)
+0.08
Earthquakes magnitude (Md)
5
3
1

FIG 6